

# Multiplicity of young isolated planetary mass objects in Taurus and Upper Scorpius

H. Bouy<sup>1,2</sup>, G. Duchêne<sup>3,4</sup>, G. Strampelli<sup>5</sup>, J. Aguilar<sup>5</sup>, J. Olivares<sup>6</sup>, D. Barrado<sup>7</sup>, S. N. Raymond<sup>1</sup>, N. Huélamo<sup>7</sup>, M. Tamura<sup>8,9,10</sup>, E. Bertin<sup>11</sup>, W. Brandner<sup>12</sup>, J.-C. Cuillandre<sup>11</sup>, P. A. B. Galli<sup>13</sup>, and N. Miret-Roig<sup>14,15,16</sup>

<sup>1</sup> Laboratoire d'astrophysique de Bordeaux, Univ. Bordeaux, CNRS, B18N, allée Geoffroy Saint-Hilaire, 33615 Pessac, France.  
e-mail: herve.bouy@u-bordeaux.fr

<sup>2</sup> Institut universitaire de France (IUF), 1 rue Descartes, 75231 Paris CEDEX 05

<sup>3</sup> Univ. Grenoble Alpes, CNRS, IPAG, 38000 Grenoble, France

<sup>4</sup> Astronomy Department, University of California Berkeley, Berkeley CA 94720-3411, USA

<sup>5</sup> Space Telescope Science Institute, 3700 San Martin Dr., Baltimore, MD 21218, USA

<sup>6</sup> Departamento de Inteligencia Artificial, Universidad Nacional de Educación a Distancia (UNED), c/Juan del Rosal 16, E-28040, Madrid, Spain

<sup>7</sup> Centro de Astrobiología (CAB), CSIC-INTA, ESAC Campus, Camino bajo del Castillo s/n, E-28692 Villanueva de la Cañada, Madrid, Spain

<sup>8</sup> Department of Astronomy, Graduate School of Science, The University of Tokyo, Tokyo, Japan

<sup>9</sup> National Astronomical Observatory of Japan, Tokyo, Japan

<sup>10</sup> Astrobiology Center, Tokyo, Japan

<sup>11</sup> Université Paris-Saclay, Université Paris Cité, CEA, CNRS, AIM, 91191, Gif-sur-Yvette, France

<sup>12</sup> Max-Planck-Institut für Astronomie, Königstuhl 17, 69117 Heidelberg, Germany

<sup>13</sup> Instituto de Astronomia, Geofísica e Ciências Atmosféricas, Universidade de São Paulo, Rua do Matão, 1226, Cidade Universitária, 05508-090 São Paulo-SP, Brazil

<sup>14</sup> Departament de Física Quàntica i Astrofísica (FQA), Universitat de Barcelona (UB), Martí i Franquès, 1, 08028 Barcelona, Spain

<sup>15</sup> Institut de Ciències del Cosmos (ICCUB), Universitat de Barcelona (UB), Martí i Franquès, 1, 08028 Barcelona, Spain

<sup>16</sup> Institut d'Estudis Espacials de Catalunya (IEEC), Edifici RDIT, Campus UPC, 08860 Castelldefels (Barcelona), Spain

Received ; accepted

## ABSTRACT

**Context.** Free-floating planetary mass objects—worlds that roam interstellar space untethered to a parent star—challenge conventional notions of planetary formation and migration, but also of star and brown dwarf formation.

**Aims.** We focus on the multiplicity among free-floating planets. By virtue of their low binding energy (compared to other objects formed in these environments), these low-mass substellar binaries represent a most sensitive probe of the mechanisms at play during the star formation process.

**Methods.** We use the *Hubble Space Telescope* and its Wide Field Camera 3 and the *Very Large Telescope* and its ERIS adaptive optics facility to search for visual companions among a sample of 77 objects members of the Upper Scorpius and Taurus young nearby associations with estimated masses in the range between approximately 5–33  $M_{\text{Jup}}$ .

**Results.** We report the discovery of one companion candidate around a Taurus member with a separation of  $111.9 \pm 0.4$  mas, or  $\sim 18$  au assuming a distance of 160 pc, with an estimated primary mass in the range between 3–6  $M_{\text{Jup}}$  and a secondary mass between 2.6–5.2  $M_{\text{Jup}}$ , depending on the assumed age. This corresponds to an overall binary fraction of  $1.8^{+2.6}_{-1.3}\%$  among free-floating planetary mass objects over the separation range  $\geq 7$  au. Despite the limitations of small-number statistics and variations in spatial resolution and sensitivity, our results, combined with previous high-spatial-resolution surveys, suggest a notable difference in the multiplicity properties of objects below  $\sim 25 M_{\text{Jup}}$  between Upper Sco and Taurus. In Taurus, five companions were identified among 78 observed objects ( $4.9^{+2.8}_{-2.0}\%$ ), whereas none were found among 97 objects in Upper Sco ( $\leq 1.2\%$ ).

**Key words.** giant planet formation, brown dwarfs

## 1. Introduction

Free-floating planetary mass objects (FFPs), also called isolated planetary mass-objects (IPMOs), are planetary-mass objects that do not orbit a star, but roam the galaxy isolated. They are some of the most challenging astrophysical objects to study: incapable of sustaining nuclear fusion, they are intrinsically extremely faint and steadily fade over time to become very difficult to detect directly. Young FFPs with super-Jovian masses in star form-

ing regions had been discovered using early direct imaging (e.g. Tamura et al. 1998; Lucas & Roche 2000; Zapatero Osorio et al. 2000). In contrast, less-massive FFPs had been discovered using indirect methods: gravitational micro-lensing surveys have proven particularly successful to detect them down to a few Earth masses (e.g. Mróz et al. 2017, 2020; Ryu et al. 2021; Sumi et al. 2023, and references therein). The future *Roman* Space Telescope will be sensitive to FFP down to masses as low as  $0.1 M_{\oplus}$  and is predicted to harvest tens of such objects during the course

of its micro-lensing survey (Johnson et al. 2020). The advent of large and very deep ground-based surveys led to the discovery of several hundreds FFP candidates in nearby star forming regions (Peña Ramírez et al. 2012; Scholz et al. 2012; Mužić et al. 2011, 2015; Bayo et al. 2011; Esplin & Luhman 2019; Miret-Roig et al. 2022, and references therein) and the field (Delorme et al. 2008, 2017). The WISE survey (Wright et al. 2010) and its subsequent extensions led to the discovery of several FFPs in the solar neighborhood (Beichman et al. 2013; Schneider et al. 2016). More recently the JWST and Euclid missions are starting to reveal large samples of FFPs thanks to their unprecedented sensitivities in the infrared (Bouy, H. et al. 2025; Luhman et al. 2024; Martín et al. 2024; Langeveld et al. 2024; De Furio et al. 2024, 2025).

The origin and the formation of FFP remains poorly understood. Even though they represent a very small fraction of the total baryonic mass of our galaxy, they add up to at least 2 to 5% of the astrophysical objects populating the Milky Way (Miret-Roig et al. 2022), making them more numerous than stars with masses greater than  $3 M_{\odot}$ . Similar to slightly more massive brown dwarfs, several scenarios are considered to explain their existence:

- a scaled-down version of star formation through gas cloud direct collapse and turbulent fragmentation (Padoan & Nordlund 2004; Hennebelle & Chabrier 2008);
- formation within a proto-planetary disc, either like gas-giant planets through core accretion (Pollack et al., 1996) or like companions through gravitational fragmentation of massive extended discs (Boss 1998), followed by ejection by dynamical scattering between planets in both cases (Veras & Raymond 2012);
- as aborted stellar embryos ejected from a stellar nursery before the hydrostatic cores could build up enough mass to become a star (Reipurth & Clarke 2001);
- through the photo-erosion of a pre-stellar core by stellar winds from a nearby OB star before it can accrete enough mass to become a star (Whitworth & Zinnecker 2004)
- within dense filaments produced by very close encounters between gaseous protoplanetary disks (Fu et al. 2025).

While recent direct observational evidence confirms that these different processes are at work (Miret-Roig et al. 2022; Palau et al. 2024; Bouy et al. 2009, and references therein), we still do not understand their relative contributions to the overall FFP population (e.g., photo-erosion can only occur in the direct vicinity of relatively scarce OB stars) and how the environment affects their outcome.

Historically, multiple systems have been commonly used to test and constrain the theories and simulations of formation and evolution. Multiple systems are indeed key diagnostics of star formation in general and of BDs and FFPs in particular. According to theory and simulations, multiple systems of isolated planetary mass objects are difficult to form and easy to break (Bate 2012). The main formation scenarios for FFP allow only few ( $<15\%$ ) and tight ( $<10$  au) binaries to form or survive. In the ejection scenario (from a disc, a planetary system or a cluster), most primordial binaries would indeed be disrupted by dynamical interactions and only systems with the highest binding energy survive, resulting in a strong preference for tighter separations and higher mass ratios. In the core-collapse scenario, the multiplicity properties are expected to follow the trends seen for more massive objects, with a binary frequency decreasing with

decreasing primary mass, a semi-major axis distribution peaking at closer separations and mass ratios shifting towards unity (Duchêne & Kraus 2013; Offner et al. 2023).

Based on these considerations, FFP binaries should be rare and tight and hence difficult to detect. Recent observations using the *Hubble Space Telescope* did not detect any visual binaries among a sample of 33 field T and Y-dwarfs (Fontanive et al. 2023) with estimated masses in the range  $11\text{--}46 M_{\text{Jup}}$ . However, observations of some young multiple systems with primaries near or within the planetary-mass regime suggest a different scenario. Several binary candidates with primaries close to or below the planetary-mass limit exhibit surprisingly large separations and relatively small mass ratios (Close et al. 2007; Fontanive et al. 2020; Langeveld et al. 2024; Luhman 2024). This contrasts sharply with theoretical and numerical predictions, as well as with the properties of slightly more massive, older brown dwarf binaries, which have a multiplicity fraction of approximately 10–15% and a tight separation distribution centered around 3–7 au. (Duchêne & Kraus 2013; Fontanive et al. 2018; Offner et al. 2023).

Due to limited sample sizes and the absence of systematic studies, it is unclear whether the discovery of these young, wide free-floating planetary mass binaries reflects a fundamental change in multiplicity properties within the planetary-mass regime or at younger ages, represents rare systems uncharacteristic of the broader FFP binary population, or is merely the result of observational biases favoring large separations. To answer these questions, we investigate the multiplicity among a sample of 77 young FFP and BD members of the Taurus and Upper Scorpius (USco) associations using the *Hubble Space Telescope* (HST) and the *Very Large Telescope* (VLT).

## 2. Targets

### 2.1. HST targets

We selected 30 targets in the USco sample of FFPs from Miret-Roig et al. (2022), and 30 targets in the sample of Taurus brown dwarfs and FFP candidates from Esplin & Luhman (2019) and Bouy et al. (in prep.). The latter used the same methodology and strategy as Miret-Roig et al. (2022) based on proper motions and multi-wavelength photometry in the Taurus molecular clouds to identify high-probability candidate members down to a few Jupiter masses only. Figure 1 shows ( $i$ ,  $i-z$ ) colour-magnitude diagrams of the targets in each region. In USco, we randomly selected targets below the planetary mass limit plus 3 mag of extinction, to minimize contamination by reddened more massive objects. The same strategy was initially used for the Taurus sample, but the lack of suitable HST guide stars in the much sparser Taurus region forced us to drop some targets in favor of slightly more massive objects with guide stars available.

Recent *Gaia* results have revealed that the various subgroups within these two associations span a wide range of distances—from 130 to 200 pc, with an average around 140 pc—and cover ages of approximately 1–10 Myr in Taurus and 3–20 Myr in USco (Galli et al. 2019; Ratzenböck et al. 2023). Our targets lack sufficient data (specifically parallax and radial velocity measurements) to determine their precise subgroup membership. Therefore, for the purposes of this study and in all subsequent figures, we adopt an average distance of 140 pc for both samples, and assume ages of 3 Myr for the Taurus targets and 5 Myr for those in Upper Sco.

The USco targets thus sample the mass range between  $6\text{--}11 M_{\text{Jup}}$  and the Taurus sample between  $5\text{--}33 M_{\text{Jup}}$ , estimated

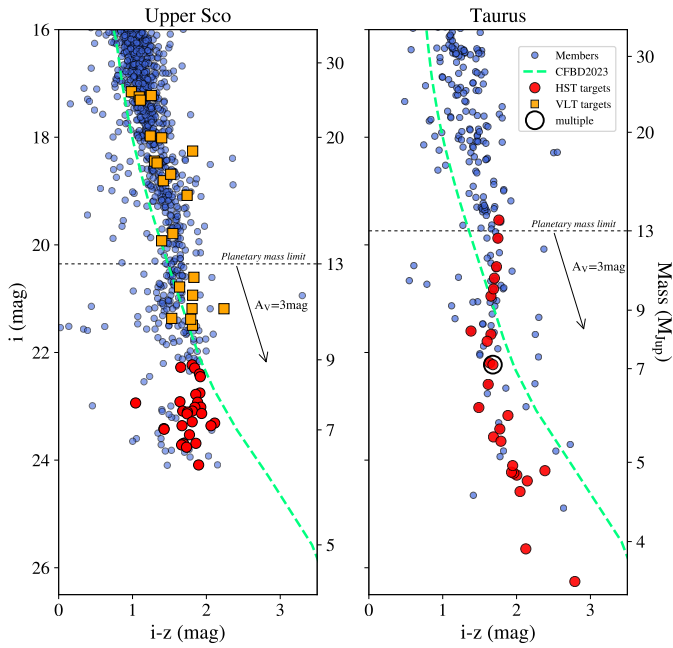


**Fig. 1.** ( $i$ ,  $i-z$ ) diagram of USco members (left) identified by Miret-Roig et al. (2022) and Taurus members (right) from Esplin & Luhman (2019), represented as blue dots. The HST targets are over-plotted as red dots and the VLT targets are orange squares. The Chabrier et al. (2023) isochrones at respectively 5 and 3 Myr and 140 pc are represented by green dashed lines and the corresponding masses are indicated on the right vertical axis. A reddening vector  $A_V=3$  mag is also represented, and the planetary mass limit of  $13 M_{Jup}$  is indicated. The new binary candidate identified in Taurus is over-plotted as a black open circle.

following the method described in Miret-Roig et al. (2022) by analyzing the available multi-wavelength photometry with *Sakam* (Romero 2019) and the ages and distances mentioned above. Figures 2 and 3 show that the targets are randomly distributed in each association and form a representative sample of the overall associations and the sub-groups composing them.

## 2.2. VLT targets

We selected 60 targets from the USco free-floating planet sample identified by Miret-Roig et al. (2022), distinct from the HST sample described above, based upon the availability of a sufficiently bright reference star for the adaptive optics wavefront sensor within  $15''$ . The selection was also designed to cover the  $12\text{--}30 M_{Jup}$  mass range, complementing the HST sample mentioned earlier and prior brown dwarf multiplicity studies in USco by Bouy et al. (2006); Kraus et al. (2006); Biller et al. (2011); Kraus & Hillenbrand (2012).

## 3. Observations and data reduction

### 3.1. HST WFC3/UVIS

Each target was observed with the UVIS channel of the WFC3 in the F814W and F850LP filters (program GO 17167, P.I. Bouy). A series of four 178 s exposures per filter was acquired, utilizing the maximum time available within a single HST orbit. Three visits failed because the Fine Guidance Sensors lost lock on the guide stars, and the corresponding data is useless. Two faint targets were not or barely detected and are also discarded in the

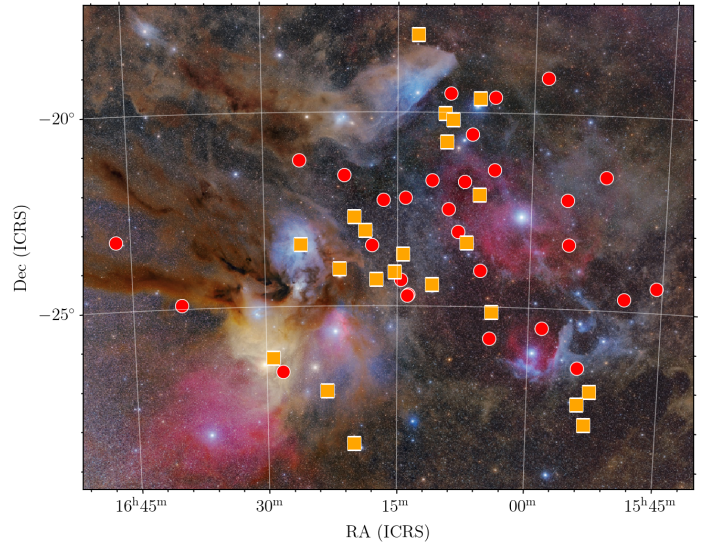


**Fig. 2.** Positions of the USco targets on a color photograph showing the clouds and nebulae. HST targets are represented with red dots and VLT targets with orange squares. Background photograph credit: Mario Cogo.

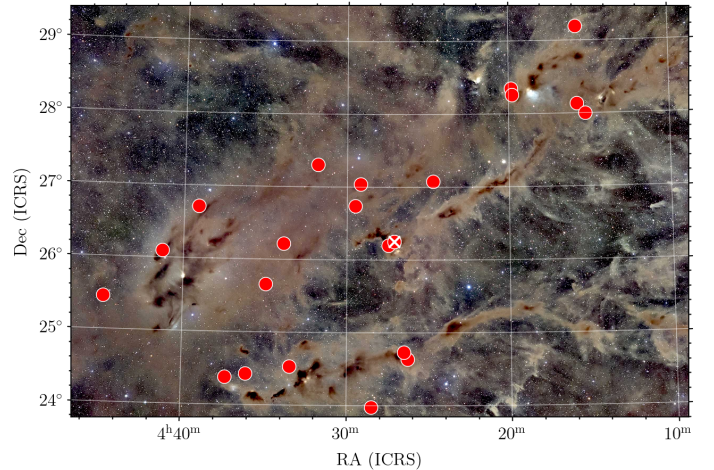


**Fig. 3.** Positions of the Taurus targets on a color photograph showing the main Taurus molecular clouds. HST targets are represented with red dots and the new binary candidate is indicated with a white cross. Background photograph credit: Chris McGrew

rest of the analysis. The final observed sample thus adds up to 30 targets in USco and 25 in Taurus.

We retrieved the pipeline processed data from the MAST archive, and used the FLC products corresponding to the calibrated individual exposure including charge transfer efficiency (CTE) correction, and the DRC products corresponding to the drizzled FLC individual images corrected for geometric distortion. We evaluated the peak signal-to-noise (S/N) of each object by quadratically combining Poisson noise based on the pixel counts and the background noise, estimated as the standard deviation in a surrounding annulus. Most targets are detected with  $20 \leq S/N \leq 50$  (median values of 28 and 26 in the F814W and F850LP filters, respectively), with a few outliers at both ends of the brightness distribution of our targets.

Because all objects were observed with the same observing sequence, we expect to achieve a similar sensitivity for wide companions, where background noise dominates the noise bud-



get. To evaluate this, we performed injection-and-recovery of companions at wide separations ( $\geq 0''.2$ ) spanning broad ranges of magnitudes and random position angles around the targets. We test the detectability of companions based on a  $5\sigma$  threshold after least squares subtraction of a single star from these mock-up binaries. From these, we compute the companion magnitude for which we achieve a 50% probability detectability (as a function of position angle). We find that the detection limit for wide companions is at  $26.5 \pm 0.4$  mag and  $26.3 \pm 0.3$  mag in the F814W and F850LP filters, respectively, corresponding to a fraction of a Jupiter mass at the ages and distances of Taurus and USco.

### 3.2. VLT ERIS/NIX

Observations with the *Enhanced Resolution Imager and Spectrograph* (ERIS) adaptive optics (AO) instrument and its NIX imager (Davies et al. 2023) were conducted at the VLT in queue mode for 25 of the 60 targets between April and December 2023 as part of program 111.24H3 (P.I. Bouy). However, due to insufficient data quality in 3 cases, the final dataset comprised 22 objects. Table 5 gives a summary of their properties as reported in Miret-Roig et al. (2022). Figure 2 shows their positions in the association, and Figure 1 shows their positions in a  $(i, i-z)$  color-magnitude diagrams. The targets were too faint for the wavefront sensor and nearby ( $< 15''$ ) bright (Gaia RP  $< 16.5$  mag) stars were used as reference for the adaptive optics. NIX has a pixel scale of 13 mas, and the observations were conducted in the J band, which provides an optimal balance between sensitivity to the cool, red targets and spatial resolution. Each target was observed with 5 DIT of 5 s exposures at 9 jittered positions, resulting in a total on-source exposure time of 225 s per target. Raw images and associated calibration frames were retrieved from the ESO archive, and the data was processed using the official ESO ERIS pipeline (v1.7.0). Table 5 reports the Strehl ratios of the observations, ranging between 2 and 32%.

## 4. Identification of companions

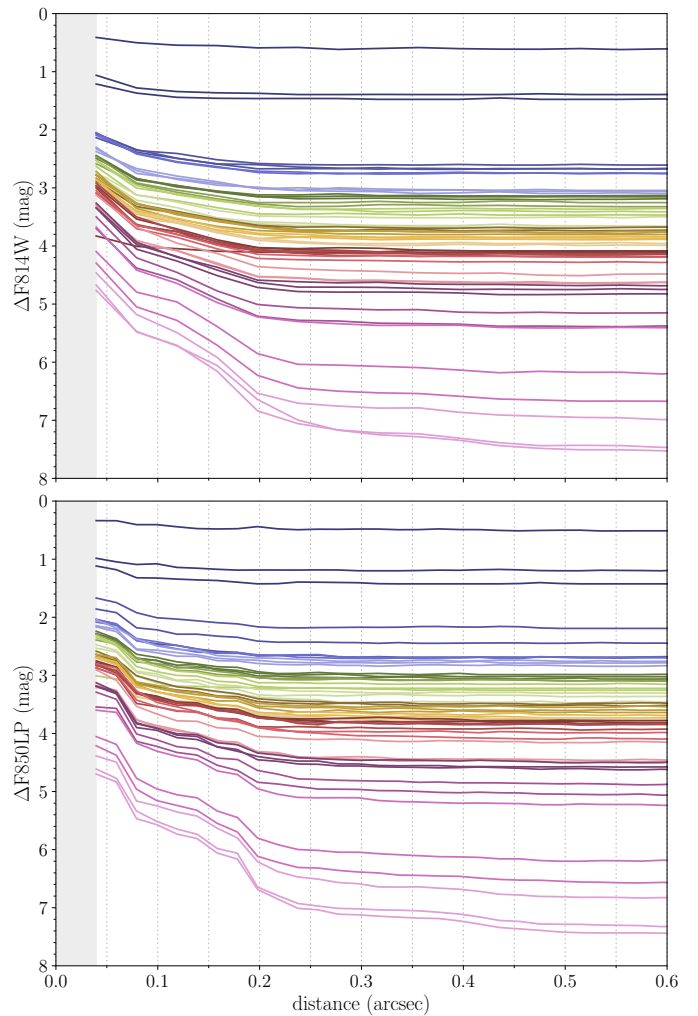
### 4.1. HST images

Figure 4 shows the detection limits determined by computing the average  $3\sigma$  rms noise along the radial profile of each object in the two filters. It shows that, in most cases, our observations are sensitive enough to detect companions with a flux ratio of  $\sim 0.5$  ( $\Delta\text{mag} = 0.75$  mag) at separations as small as  $0''.05$  (or approximately 7 au at the distance of USco and Taurus).

We initially visually examined all images to identify easily detectable companions, resulting in the discovery of three visual companions within  $1''$  of their primaries.

J042705.86+261520.3 was confirmed as a binary candidate with a separation of  $111.9 \pm 0.4$  mas, as illustrated in Fig. 5. Table 1 presents the relative astrometry and flux ratio measured in the F814W and F850LP images, while Table 2 provides the individual component photometry in the two HST filters. J042705.86+261520.3 lies in close proximity, in projection, to the filamentary structure containing clumps B211, B231, B216, B217, and B218, which is connected to LDN1495 and corresponds to Group 8 in Galli et al. (2019), located at an average distance of 160 pc. If this distance is assumed, the measured angular separation translates to a physical separation of approximately 18 au.

We estimated component masses by linearly interpolating the predicted values from the Chabrier et al. (2023) models for ages of 1 Myr and 3 Myr, assuming a distance of 160 pc. The re-



**Fig. 4.** Detection limits in the HST F814W (top) and F850LP (bottom) images.

**Table 1.** J042705.86+261520.3AB properties

Parameter	Filter	Value	Uncertainty	Weighted Average
$\delta$ (mas)	F814W	112.5	0.4	$111.9 \pm 0.4$
	F850LP	111.3	0.4	
P.A. ( $^\circ$ )	F814W	14.8	0.1	$13.6 \pm 0.9$
	F850LP	12.4	0.1	
flux ratio	F814W	0.702	0.005	
	F850LP	0.761	0.003	

**Table 2.** J042705.86+261520.3 A and B properties

Component	F814W (mag)	$\sigma_{\text{F814W}}$ (mag)	F850LP (mag)	$\sigma_{\text{F850LP}}$ (mag)	Mass ( $M_{\text{Jup}}$ )
A	21.92	0.02	21.03	0.02	3–6
B	22.30	0.02	21.33	0.02	2.6–5.2

sulting mass range for each component is listed in Table 2. These values should be considered lower limits, as extinction could increase them. For instance, assuming a visual extinction of  $A_V = 3$  mag would yield a primary mass range of 5–10  $M_{\text{Jup}}$  and a secondary mass range of 4.5–9  $M_{\text{Jup}}$ . In any case, the mass ratio is relatively high, approximately 0.9.

J042911.69+270220.2 displayed a visual companion of similar luminosity and color located  $1''$  north. However, the source

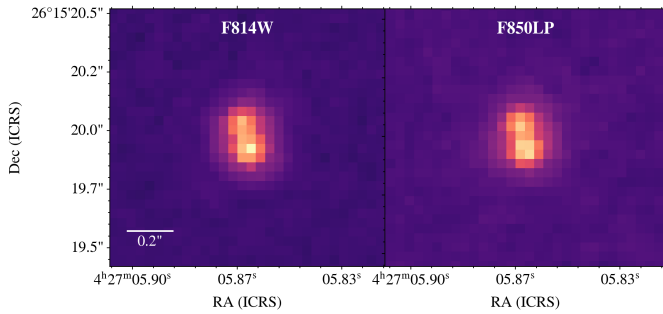


**Fig. 5.** HST F814W (left) and F850LP (right) images of the companion identified around J042705.86+261520.3 through direct inspection. A square root stretch is used. North is up and east is left.

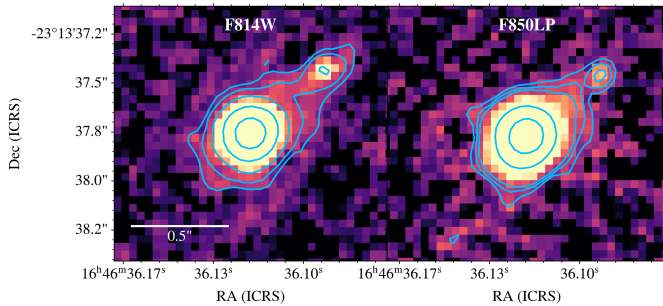


**Fig. 6.** HST F814W (left) and F850LP (right) images of the visual companion identified around J164636.12-231337.6 through direct inspection. A square root stretch is used. Contours highlight the extended emission originating from the visual companion. North is up and east is left.

is detected and reported in Bouy et al. (in prep.) ground-based images. It displays a proper motion measurement ( $\mu_\alpha \cos \delta, \mu_\delta$ ) =  $(6.9, 3.1) \pm (3.6, 3.6)$  mas yr<sup>-1</sup> inconsistent with the primary's motion of  $(\mu_\alpha \cos \delta, \mu_\delta)$  =  $(6.9, -14.9) \pm (2.5, 2.5)$  mas yr<sup>-1</sup>, leading us to discard it as a background or foreground coincidence given that this difference in proper motion is too large to be orbital motion.

J164636.12-231337.6 features a faint object (3% of the target's brightness) at approximately 0''.5 separation, as shown in Fig. 6. The companion's color and luminosity, shown in Figure 9, were significantly bluer than those of targets with similar luminosities. Additionally, the images revealed extended nebulousity roughly aligned with the companion's position angle (Fig. 6). This, combined with its bluer color, suggested the companion could be a background galaxy, especially given the lower extinction in USco compared to Taurus. Based on these factors, the companion to J164636.12-231337.6 was rejected as a likely background galaxy.

We estimate the probability of finding a galaxy close to the 55 targets of our sample using the COSMOS 2020 catalog (Weaver et al. 2022) that includes deep HST ACS observations in the F814W filter (Koekemoer et al. 2007). We used their 1ptype star/galaxy discriminator to select only the galaxies, and computed the probability to find a galaxy within radii of 0''.5 and 1''.0 over the magnitude range between each target F814W magnitude and the limit of sensitivity of our images computed as described above and estimated at 26.5 mag in the F814W. We find that we expect to detect between  $\sim 1$  and  $\sim 4$  galaxies within radii of respectively 0''.5 and 1''.0 among our sample of 55 objects.

To identify additional companions closer to the PSF core, we then applied three different PSF subtraction methods that take advantage of the remarkable stability provided by HST.

#### 4.1.1. Least-squares fit with a natural PSF (PSFsub)

The initial approach involved a straightforward least-squares adjustment. Since BDs and FFPs are significantly redder than most field stars and to avoid any chromatic effect, we opted to use images of our own targets as reference PSFs. Specifically, we selected the four brightest targets (see Table 4) and used each of them as a PSF to subtract from all other targets. This strategy was designed to minimize systematic artifacts that could arise from a faint companion associated with an individual reference PSF. One drawback of using observations from different visits is the "breathing" effect of the HST—small variations in focus position that lead to subtle changes in the wings of the PSF (Hasan & Bely 1994). As a result, for each target, we generated eight PSF-subtracted images, four per filter, and only considered candidate companions that are consistently identified using multiple PSF stars.

#### 4.1.2. *StraKLIP*

A second avenue of analysis uses principle component analysis to model and subtract the stellar PSFs with the software packages *StraKLIP*<sup>1</sup> (Strampelli et al. 2022) and *PUBLIC-WiFi* (described 4.1.3). *StraKLIP* is a pipeline originally developed to detect and characterize close-in candidate companions to stars in HST/WFC3-IR and ACS datasets. For this study, its capabilities have been expanded to include the WFC3-UVIS dataset and to enable a more robust analysis of candidate companions.

Briefly, *StraKLIP* performs the following five fundamental steps:

1. **Postage stamp creation:** Small *postage-stamp* images (also referred to as *tiles*) are generated for each source in the *input catalog*. These images define the search regions,  $\mathcal{S}$ , that will be inspected for each target.  $\mathcal{S}$  must be large enough to encompass the bright wings of the PSF while remaining small enough to avoid contamination from the wings of nearby catalog sources.
2. **KLIP analysis:** PSF subtraction is performed for each source in each *tile* using a set of local stars to construct a reference differential imaging (RDI) PSF library for the KLIP algorithm (Soummer et al. 2012).
3. **Residual detections:** S/N maps of the PSF-subtracted *residual tiles* are analyzed to identify previously undetected astronomical signals. To be classified as a candidate, a detection must meet two criteria: (i) it must appear at a minimum significance level of 5 S/N, and (ii) it must be present across multiple consecutive KLIP modes to rule out artifacts.
4. **Candidate validation:** for non visual binaries, jack-knife tests are performed to insure that these candidates are not artifacts introduced by one of the reference images. This test is performed by subtracting the target with a PSF library where one at the time one reference is removed, and by analyzing each single residual. If the candidate disappears in one of them, that's a clear sign that was injected, and therefore not real.
5. **Candidate extraction:** PSFs forward modeling through the subtraction process (Pueyo 2016) are combined with Markov

<sup>1</sup> <https://github.com/strampelligiovanni/StraKLIP>

Chain Monte Carlo (MCMC) algorithms to extract validated candidate detections and determine key parameters, such as contrast, position angle, and separation relative to the primary target. Additionally, the sensitivity of the mass-separation parameter space is quantified through contrast curves, providing insights into occurrence rates.

#### 4.1.3. *PUBLIC-WiFi*

*PUBLIC-WiFi* (Previously *Undiscovered Binaries Lying In Clusters - Wide Field*)<sup>2</sup>, like *StraKLIP*, is a principal component analysis (PCA)-based faint companion detection pipeline designed to organize the analysis of large wide-field surveys of unocculted point sources. The main points of difference are in architecture – *PUBLIC-WiFi* is primarily object-oriented where *StraKLIP* is primarily database-oriented – and in some specifics of implementation, e.g. how PSF forward modeling is implemented (Wang et al. 2015a; Pueyo 2016; Ruffio et al. 2017). Though the two algorithms necessarily share many of the same basic steps described in 4.1.2, they nevertheless provide semi-independent checks on each other with regard to companion detection and search depth.

*PUBLIC-WiFi* is initialized with an input catalog containing, at minimum, columns for the target names, exposure identifiers, and the x- and y-coordinates of the target. If a target is detected in more than one exposure, each detection is recorded on a separate row, and further columns should be included to specify the differences between the exposures (e.g., a filter change or overlapping mosaic tile). The combination (target name, exposure identifier) should be unique, and is used to organize the PSF subtraction. The *PUBLIC-WiFi* pipeline creates an object for each target (internally called a *Star*) that aggregates the relevant catalog rows, stores the metadata for all the associated exposures, and creates a postage stamp for each instance of the target in the survey. Once all *Star* objects have been created, they are able to interface with each other to assemble reference PSF libraries for PCA-based PSF subtraction. *PUBLIC-WiFi* currently uses the pyKLIP implementation of the KLIP algorithm (Soummer et al. 2012), but is well-suited to integrate other algorithms that combine images from a reference library to construct PSF models, such as LOCI (Lafrenière et al. 2007) or NMF (Ren et al. 2018). Finally, wide-field surveys can contain tens or even hundreds of targets, presenting a significant challenge when it comes to synthesizing the analysis results in a sensible way. *PUBLIC-WiFi* provides a useful browser-based data exploration interface for organizing, displaying and analyzing the resultant data products that allows the user to isolate each target and scroll through the related data products including the reference library used, post-subtraction residuals, SNR maps, matched filtering results, and more. A more complete description of *PUBLIC-WiFi* will be provided in a future publication.

#### 4.1.4. Tentative candidates

The three methods were employed to identify companion candidates and characterize their positions and fluxes. We note that *StraKLIP* and *PUBLIC-WiFi* are based on similar fundamental principles and are expected to yield consistent results. Despite their similarities, we report the results from both methods, as they serve as an important sanity check and contribute to the robustness of our analysis.

**Table 3.** Properties reported by *StraKLIP* for the faint companion candidates

Object	$\delta$ (mas)	P.A. (°)	Flux ratio (F850LP)
J160539.08-240333.0	701.3	225	0.03
J164636.12-231337.6	65.6	151	0.04
J160412.34-212747.2	227.6	106	0.05
J043606.80+242549.5	85.6	166	0.05

The three methods successfully recover J042705.86+261520.3 and identify 3 tentative detections in the F850LP filter around J043606.80+242549.5, J164636.12-231337.6, J160412.34-212747.2, and one clear detection at larger separation around J160539.08-240333.0. Their properties reported by *StraKLIP* are given in Table 3. Figure 7 shows the residuals after modeling by the three methods.

Two of these four new candidates exhibit relatively large separations, while all four have very small flux ratios of just 3–5%. If confirmed, these systems would be unusual compared to the known mass ratio distribution of slightly more massive ultracool dwarfs, which peaks around near-equal masses.

However, in some cases, the detections fall close to or even below the nominal 5- $\sigma$  threshold in one or several methods, and in two instances, they are at or below the Nyquist sampling limit, making them tentative. Due to their uncertain nature and the lack of F814W measurement, we do not include them in the subsequent analysis.

#### 4.2. VLT images

Detecting companions in AO images is significantly more challenging than in HST images. The shape of the point-spread function (PSF) is influenced not only by the seeing conditions but also by the brightness and distance of the wavefront reference star from the target. In our case, all targets were indeed too faint for direct wavefront sensing, making the observations particularly susceptible to tip-tilt anisoplanatism. As a result, most objects appear slightly elongated in the direction of the tip-tilt reference star. Furthermore, the observations were conducted in queue mode, spread over multiple nights, leading to substantial variations in image quality between nights and even within individual nights. Given that the AO correction was generally moderate, we did not attempt PSF subtraction to search for faint companions within the PSF core as was done for the HST data, because constructing a reliable PSF model for subtraction was not feasible.

Instead, we limited our analysis to a visual inspection of the images. Figure 8 shows that, in most cases, our observations should have also been sensitive enough to detect companions with a flux ratio of  $\sim 0.5$  ( $\Delta J=0.75$  mag) at separations as small as 0''.05 (or approximately 7 au at the distance of Taurus and USco). This sensitivity is comparable to that achieved in previous studies of the same association for similar ultracool objects by Bouy et al. (2006); Kraus et al. (2006); Biller et al. (2011); Kraus & Hillenbrand (2012) and to the HST images presented above. This inspection did not reveal any companions within 0''.6 of the 22 targets. Companions at larger separations would have been detected and reported in Miret-Roig et al. (2022) as common proper-motion companions.

<sup>2</sup> [https://github.com/aggle/public\\_wifi](https://github.com/aggle/public_wifi)

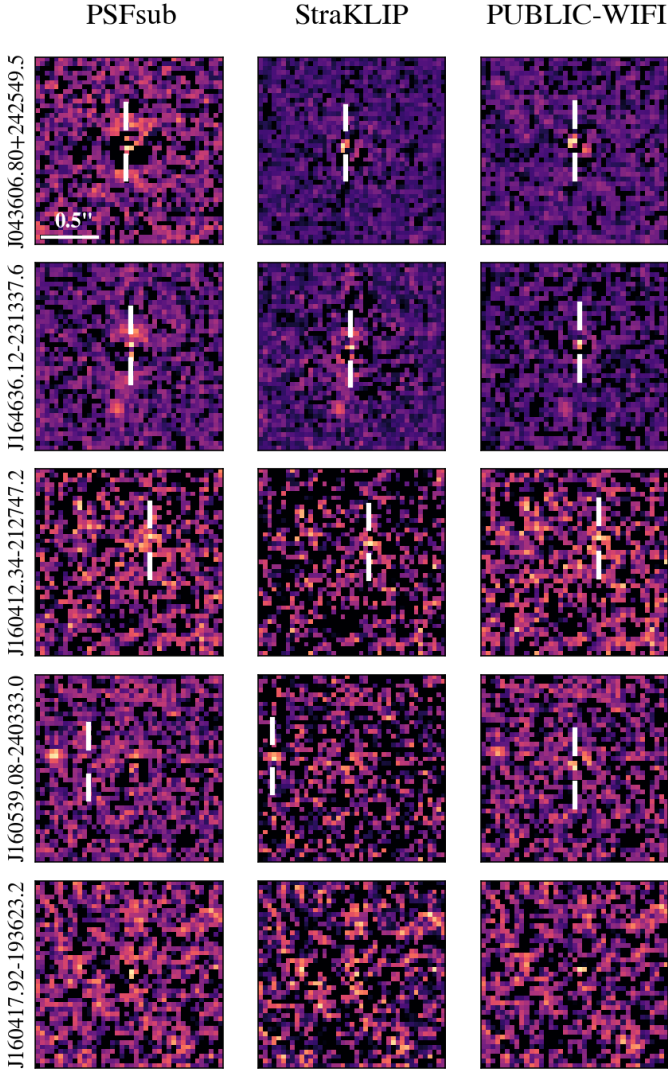


**Fig. 7.** Residuals for J043606.80+242549.5, J164636.12-231337.6, J160412.34-212747.2, and J160539.08-240333.0 in the F850LP filter, obtained using the three methods described in the text. The scale is indicated in the top-left image, with crosshairs marking the detection locations. For comparison, the residuals of an unresolved target (J160417.92-193623.2) are shown in the bottom row. The suspected galaxy is also visible in J164636.12-231337.6 images (see also Fig. 6). The orientation is in native detector coordinates.

## 5. Discussion

### 5.1. Multiplicity statistics

In this section we discuss the result obtained with the HST survey only, which is homogeneous in sensitivity and spatial resolution. The detection of 1 candidate among a sample of 55 objects leads to an overall binary fraction of  $1.8^{+2.6}_{-1.3}\%$ , computed using Bayesian inference for a binomial proportion. This number is consistent with the values reported for slightly more massive objects in the field (Burgasser et al. 2006; Fontanive et al. 2018, 2023).

With only one detected binary, it is not possible to derive meaningful statistics on the distributions of separation and mass ratio. Nevertheless, we note that we did not identify any wide<sup>3</sup>

<sup>3</sup> wide meaning with a separation larger than  $\gtrsim 30$  au corresponding to  $5\text{-}\sigma$  of the separation distribution reported for field late-T and Y dwarfs (Fontanive et al. 2018)

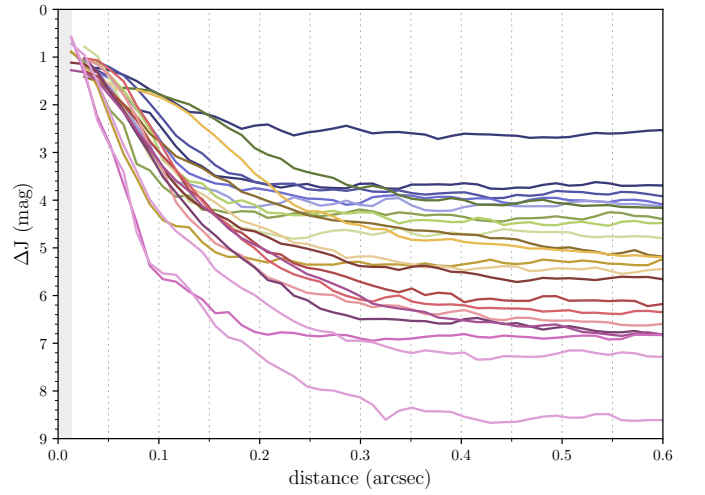


**Fig. 8.** Same as Fig. 4 for the VLT ERIS J-band images, computed using 2-pixel (26 mas) increments.

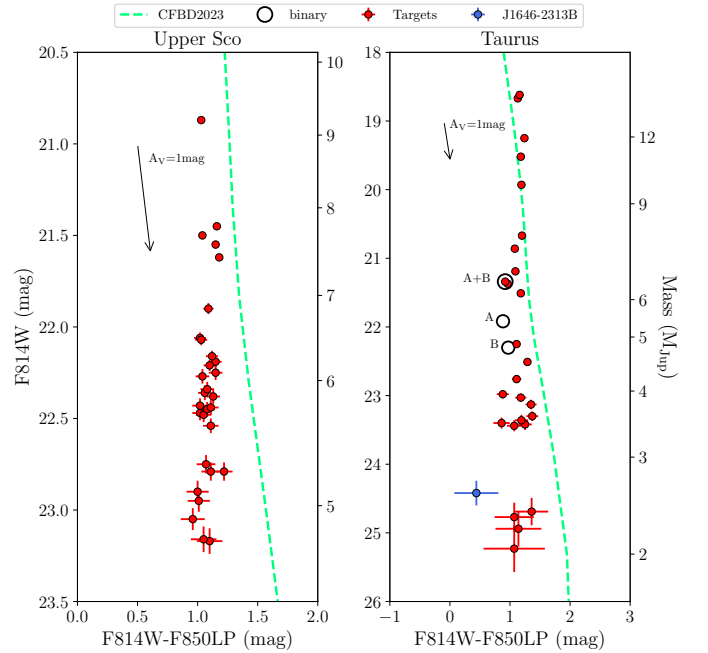


**Fig. 9.** (F814W, F814W-F850LP) diagram of USco targets (left panel) and Taurus targets (right). The Chabrier et al. (2023) isochrones at resp. 5 and 3 Myr and 140pc are represented (green line) and the corresponding masses are indicated on the right vertical axis. The combined photometry (A+B) and individual components (A, B) of the binary candidate J042705.86+261520.3 are overplotted as labeled black open circles. The suspected background galaxy located 0'5 from J164636.12-231337.6 is indicated as a blue dot. A reddening vector  $A_V=1$  mag is also represented.

binaries among the HST targets and VLT targets below the planetary mass limit, compatible at  $1\text{-}\sigma$  credible interval with a wide binary fraction of up to  $\leq 1.8\%$ <sup>4</sup>. The separation of the binary candidate is close to the resolution limit of HST observations, suggesting that we may be missing the bulk of the FFP binary population. Although challenging with current instrumentation, higher spatial resolution observations are needed to explore the currently unprobed separation range below 7 au. We also note

<sup>4</sup> determined using Bayesian inference for a binomial proportion



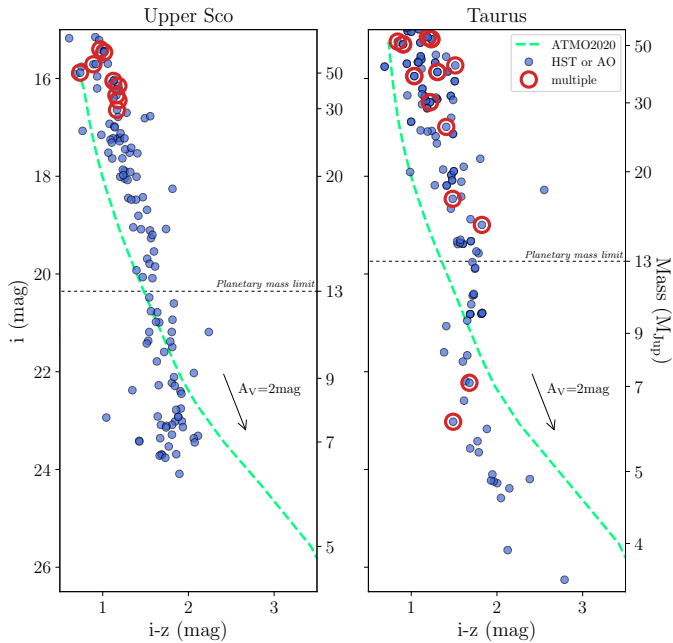


**Fig. 10.** (*i*, *i*-*z*) diagram of USco members (left panel) and Taurus members (right) observed at high spatial resolution using either HST or adaptive optics (blue dots) by Todorov et al. (2010, 2014); Bouy et al. (2006); Biller et al. (2011); Kraus & Hillenbrand (2012); Kraus et al. (2006); Konopacky et al. (2007); Luhman et al. (2007, 2009) as well as this work. The Chabrier et al. (2023) isochrones at respectively 5 and 3 Myr and 140pc are represented by a green dashed line and the corresponding masses are indicated on the right vertical axis. The resolved binary is over-plotted as a red open circle. A reddening vector  $A_V=2$  mag is also represented.

that the candidate exhibits a relatively "common" and near-equal mass ratio compared to the distribution observed for older and slightly more massive objects in the field (Burgasser et al. 2006; Fontanive et al. 2018, 2023).

## 5.2. Dependence on environmental conditions

If considering the Taurus sample only, from which the binary candidate comes from, the binary fraction rises to  $3.8^{+5.2}_{-2.8}\%$  in Taurus while the lack of companion candidate among 30 objects in USco is compatible at  $1-\sigma$  credible interval with a binary fraction of up to  $\leq 3.6\%$ . The difference between the two regions is not statistically conclusive mostly because of the limited sample sizes, but it suggests a potential trend that warrants further investigation with larger samples.

In that context, Figure 10 presents (*i*, *i*-*z*) color-magnitude diagrams for objects observed at high spatial resolution in Taurus and USco using HST or adaptive optics over the past two decades, as reported in the present work and Todorov et al. (2010, 2014); Bouy et al. (2006); Biller et al. (2011); Kraus & Hillenbrand (2012); Kraus et al. (2006); Konopacky et al. (2007); Luhman et al. (2007, 2009). Both regions have been extensively studied, with statistically significant samples including over 100 sources between a few Jupiter masses and  $50 M_{\text{Jup}}$  in each association. The spatial resolution and sensitivity of these HST and AO studies are variable but comparable, typically achieving flux ratios of  $\sim 0.5$  or better at separations of about  $0''.05 \sim 0''.08$ .

Since Taurus and USco are located at similar distances (approximately 140pc) and have comparable ages, the sensitivity

of all these surveys to BD and FFP and their companions is effectively very similar for both regions. Notably, no companions have been detected in USco among the 98 objects with masses below  $\sim 25 M_{\text{Jup}}$ , corresponding to an upper limit on the binary fraction of up to  $\leq 1.2\%$ . In contrast, so far four binaries have been identified in Taurus among the 78 objects observed at high spatial resolution within the same mass range, corresponding to a binary fraction of  $4.9^{+2.8}_{-2.0}\%$  and highlighting a potentially significant difference in the population of low-mass companions between the two regions. Above  $25 M_{\text{Jup}}$  the relative numbers of multiple systems identified are statistically indistinguishable between the two associations, as already reported in the previous studies mentioned above (Bouy et al. 2006; Biller et al. 2011; Kraus & Hillenbrand 2012; Kraus et al. 2006; Konopacky et al. 2007).

## 5.3. Implications for the formation process of FFPs

The Taurus molecular clouds and USco were chosen for this study because they represent drastically different environments (Reipurth 2008a,b). While USco includes several massive B stars and around 3 500 members (Blaauw 1946; Miret-Roig et al. 2022), Taurus is a sparser T-association with no massive star and around 900 low-mass members located around/within the filamentary clouds (Galli et al. 2019; Joncour et al. 2018). USco is also slightly older, with groups ranging from 3 to 19 Myr compared to 1 to 10 Myr for Taurus.

If real, the apparent lack of binaries below  $25 M_{\text{Jup}}$  in USco could be the result of different formation pathways. A variety of formation channels for binary FFPs have been proposed, including both dynamic ejection mechanisms such as planet-planet (or BD-BD) scattering Veras & Raymond (2012); Lazzoni et al. (2024), stellar flybys Wang et al. (2024), as well as other mechanisms such as photo-erosion of fragmenting stellar cores Diamond & Parker (2024) or via grazing encounters between protoplanetary disks Fu et al. (2025). Very dynamic formation channels likely produce a lower binary population than calmer ones, and it is possible that the dominant formation channels in USco and Taurus are different. Conversely, it could be that fewer objects in the  $25 M_{\text{Jup}}$  mass range form through core-collapse in USco compared to Taurus. Core-collapse is indeed generally thought to be the main formation mechanism for these binaries, and it may be challenging to form very low-mass cores that could eventually become FFPs or low-mass BDs in denser regions with strong feedback from massive stars and their supernovae (Preibisch & Zinnecker 1999).

The difference between the two regions could instead be the result of dynamical disruption of binary FFPs by stellar encounters Parker & Quanz (2012); Yu & Lai (2024); Wang et al. (2015b); Huang et al. (2024). Simulations by Portegies Zwart & Hochart (2024) show that binary FFPs in an USco-like environment are disrupted with a half life  $\lesssim 1$  Myr. Unless they are continuously resupplied, it would not be surprising that the older and denser cluster would have a lower binary rate.

However, this simple picture—where high stellar density and feedback from massive stars prevent or disrupt binary FFPs—becomes more complex and puzzling when considering the discoveries of wide binary FFP candidates in several young, nearby massive clusters. Luhman (2024) reported the detection of one candidate binary FFP ([LAB2024] 139) among a sample of 242 BDs and FFPs identified in the 1 Myr, 400 pc Orion Nebula Cluster (ONC). This system exhibits a wide separation of 132 au and a relatively small mass ratio of  $q \sim 0.13$ . Similarly, Langeveld



et al. (2024) report two binary candidates among their 6 FFP candidates in the 1–3 Myr, 300 pc NGC 1333 cluster (NGC1333-NN10 and NGC1333-NN12). Both systems have wide separations (164 au and 76 au, respectively) but relatively "common" nearly equal mass ratios of 0.7–0.8.

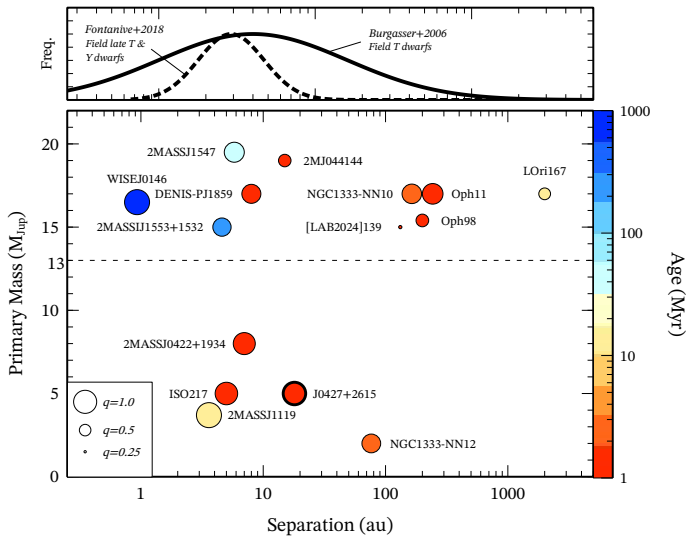


**Fig. 11.** Lower panel: Primary mass vs separation for known BD-FFP and FFP-FFP binaries or candidates. The color scale indicates the age and the size is proportional to the mass ratio. 2MASSJ 1119 data from Best et al. (2017). WISEJ0146 data from Dupuy et al. (2015). 2MASSJ044144, ISO217 and 2MASSJ0422 data from Todorov et al. (2014). DENIS-PJ1859 data from Bouy et al. (2004). Data for 2MASSJ 1547 from Calissendorff et al. (2019). Data for 2MASSJ J1553 from Dupuy & Liu (2012). Data for NGC1333-NN10 from Langeveld et al. (2024). Data for [LAB2024] 139 from Luhman (2024). Data for Oph 98 from Close et al. (2007) and for Oph 11 from Fontanive et al. (2020). Data for LOri 167 from Barrado Y Navascués et al. (2007). The new multiple system from the present study (J042705.86+261520.3) is represented with a circle with a thick edge and follows the same color and size scales. The upper panel shows the distribution of separations reported for older and slightly more massive field T-dwarfs from Burgasser et al. (2006) (solid line) and field late-T and Y dwarfs from Fontanive et al. (2018) (dashed line).

If confirmed as physical pairs, these 3 wide binary candidates with primaries at or near the planetary mass regime would join the two previously known young wide binaries Oph 11 ( $\rho = 243$  au, Close et al. 2007) and Oph 98, ( $\rho = 200$  au, Fontanive et al. 2020) located in the Ophiuchus star forming region near the  $\rho$ -Oph pair of early-B stars, as well as the 2000 au system LOri 167 made of a  $18 M_{\text{Jup}}$  and  $8 M_{\text{Jup}}$  pair in the Collinder 69 cluster near the massive  $\lambda$ -Ori pair of OB stars (Barrado Y Navascués et al. 2007), as illustrated in Fig. 11. They would also add to the similarly weakly bound wide binary BD candidates reported in Bouy et al. (2006) and Béjar et al. (2008) in USco. Notably, only one such wide binary BD has been reported to date in Taurus (FU Tau B, Luhman et al. 2009).

The ONC, NGC1333, USco, Collinder 69 and Ophiuchus all contain several massive B stars providing strong radiation and shockwaves. They are also all significantly denser than Taurus. Star formation occurs more clustered in these four regions, as opposed to Taurus where it is more distributed and occurs in isolated or small groups (Joncour et al. 2018; Galli et al. 2019). The presence of wide FFP and BD binaries in these regions therefore challenges the picture mentioned above, which suggests that higher stellar densities and/or stronger feedback from

massive stars prevent or disrupt low-mass BD and FFP binaries, particularly the wide, low-binding-energy systems. Interestingly, 2MASS J0422+1934 (Todorov et al. 2014) is in the immediate vicinity of T Tau, a region that is not particularly dense but including some of the most massive members of the TMC.

However, most of these wide systems have not yet been confirmed as physical pairs and, given the stellar densities of these clusters, they could instead be chance projections of two unbound members (Akter & Goodwin 2019) or even unrelated background sources. Confirmation of their nature is therefore necessary before drawing any firm conclusion.

## 6. Conclusion

We present high-spatial-resolution observations using HST and VLT of a sample of 38 FFPs and 14 low-mass BD members of the USco association, as well as 25 FFP members of the Taurus association. We detect one binary candidate in Taurus with a separation of  $111.9 \pm 0.4$  mas corresponding to 18 au at 160 pc, a mass ratio of 0.9 and estimated component masses in the range  $3\text{--}6 M_{\text{Jup}}$  for the primary and  $2.6\text{--}5.2 M_{\text{Jup}}$  for the secondary, according to Chabrier et al. (2023) models and assuming no extinction. No binary candidates were identified in USco and no wide binary candidates were identified in either association. Using advanced PSF-fitting methods, we also report the tentative detection of four very faint companion candidates in the F850LP filter, with flux ratios of only 3% to 5%. Given the uncertain nature of these detections, which are at the resolution and/or detection limits of the HST images, these candidates should be considered with caution and require confirmation.

When combined with previous high-spatial-resolution surveys of the very low-mass populations in these regions, our findings reveal a statistically significant difference in the multiplicity properties below  $25 M_{\text{Jup}}$ , with a binary fraction of  $4.9^{+2.8}_{-2.0}\%$  in Taurus and an upper limit of  $\leq 1.2\%$  in USco.

On one hand, the absence of FFP binaries in USco and their presence in Taurus suggest that dynamical interactions, higher stellar densities, and/or feedback from massive stars in USco likely prevent the formation or disrupt fragile binary systems at the lowest masses.

On the other hand, the existence of a few BD and FFP wide binary candidates reported in the literature in USco and other dense clusters including massive stars—such as the ONC, NGC 1333, Collinder 69 and Ophiuchus—appears to contradict this picture. If their binary nature is confirmed, the presence of such wide systems in these regions suggests that either some FFP binaries can survive despite strong dynamical processing (Portegies Zwart & Hochtart 2024; Huang et al. 2024) or that certain conditions—such as lower-density subregions within these clusters—allow them to persist.

This paradox highlights the sensitivity of low-mass BD and FFP formation to inborn and evolutionary effects. It raises new questions about the exact role of environmental factors in shaping the low-mass BD and FFP population and underlines the need for further observational confirmation of the physical nature of these wide systems. Additionally, future observations at higher spatial resolution, particularly targeting the unexplored separation range below 7 au, will be crucial to providing a more complete picture of how environmental factors contribute to the formation and evolution of low-mass objects.

**Acknowledgements.** We are grateful to Tricia Royle for her support with the HST observations. JO acknowledge financial support from "Ayudas para contratos posdoctorales de investigación UNED 2021". DB and NH have been funded

by grant No. PID2023-150468NB-I00 by the Spain Ministry of Science, Innovation/State Agency of Research MCIN/AEI/ 10.13039/501100011033 and by “ERDF A way of making Europe”. PABG acknowledges financial support from the São Paulo Research Foundation (FAPESP) under grant 2020/12518-8. This research has made use of the VizieR catalogue access tool, CDS, Strasbourg, France. The original description of the VizieR service was published in Ochsenbein et al. (2000). This research made use of Photutils, an Astropy package for detection and photometry of astronomical sources (Bradley et al. 2025). This work made use of GNU Parallel (Tange 2011), astropy (Astropy Collaboration et al. 2013; Price-Whelan et al. 2018), Topcat (Taylor 2005), matplotlib (Hunter 2007), Plotly (Plotly Technologies Inc. 2015), Numpy (Harris et al. 2020), aplpy (Robitaille & Bressert 2012; Robitaille 2019).

## References

- Akter, S. & Goodwin, S. P. 2019, *MNRAS*, 488, 3446
- Astropy Collaboration, Robitaille, T. P., Tollerud, E. J., et al. 2013, *A&A*, 558, A33
- Barrado Y Navascués, D., Bayo, A., Morales-Calderón, M., et al. 2007, *A&A*, 468, L5
- Bate, M. R. 2012, *MNRAS*, 419, 3115
- Bayo, A., Barrado, D., Stauffer, J., et al. 2011, *A&A*, 536, A63
- Beichman, C., Gelino, C. R., Kirkpatrick, J. D., et al. 2013, *ApJ*, 764, 101
- Béjar, V. J. S., Zapatero Osorio, M. R., Pérez-Garrido, A., et al. 2008, *ApJ*, 673, L185
- Best, W. M. J., Liu, M. C., Dupuy, T. J., & Magnier, E. A. 2017, *ApJ*, 843, L4
- Biller, B., Allers, K., Liu, M., Close, L. M., & Dupuy, T. 2011, *ApJ*, 730, 39
- Blaauw, A. 1946, PhD thesis, -
- Boss, A. P. 1998, *Earth Moon and Planets*, 81, 19
- Bouy, H., Brandner, W., Martín, E. L., et al. 2004, *A&A*, 424, 213
- Bouy, H., Huélamo, N., Martín, E. L., et al. 2009, *A&A*, 493, 931
- Bouy, H., Martín, E. L., Brandner, W., et al. 2006, *A&A*, 451, 177
- Bouy, H., Martín, E. L., Cuillandre, J.-C., et al. 2025, *A&A*, 696, A80
- Bradley, L., Sipőcz, B., Robitaille, T., et al. 2025, *astropy/photutils*: 2.1.0
- Burgasser, A. J., Kirkpatrick, J. D., Cruz, K. L., et al. 2006, *ApJS*, 166, 585
- Calissendorff, P., Janson, M., Asensio-Torres, R., & Köhler, R. 2019, *A&A*, 627, A167
- Chabrier, G., Baraffe, I., Phillips, M., & Debras, F. 2023, *A&A*, 671, A119
- Close, L. M., Zuckerman, B., Song, I., et al. 2007, *ApJ*, 660, 1492
- Davies, R., Absil, O., Agapito, G., et al. 2023, *A&A*, 674, A207
- De Furio, M., Meyer, M. R., Greene, T., et al. 2024, *arXiv e-prints*, arXiv:2409.04624
- De Furio, M., Meyer, M. R., Greene, T., et al. 2025, *ApJ*, 981, L34
- Delorme, P., Delfosse, X., Albert, L., et al. 2008, *A&A*, 482, 961
- Delorme, P., Dupuy, T., Gagné, J., et al. 2017, *A&A*, 602, A82
- Diamond, J. L. & Parker, R. J. 2024, *ApJ*, 975, 204
- Duchêne, G. & Kraus, A. 2013, *ARA&A*, 51, 269
- Dupuy, T. J. & Liu, M. C. 2012, *ApJS*, 201, 19
- Dupuy, T. J., Liu, M. C., & Leggett, S. K. 2015, *ApJ*, 803, 102
- Esplin, T. L. & Luhman, K. L. 2019, *AJ*, 158, 54
- Fontanive, C., Allers, K. N., Pantoja, B., et al. 2020, *ApJ*, 905, L14
- Fontanive, C., Bedin, L. R., De Furio, M., et al. 2023, *MNRAS*, 526, 1783
- Fontanive, C., Biller, B., Bonavita, M., & Allers, K. 2018, *MNRAS*, 479, 2702
- Fu, Z., Deng, H., Lin, D. N. C., & Mayer, L. 2025, *Science Advances*, 11, eadu6058
- Galli, P. A. B., Loinard, L., Bouy, H., et al. 2019, *A&A*, 630, A137
- Harris, C. R., Millman, K. J., van der Walt, S. J., et al. 2020, *Nature*, 585, 357
- Hasan, H. & Bely, P. Y. 1994, in *The Restoration of HST Images and Spectra - II*, ed. R. J. Hanisch & R. L. White, 157
- Hennebelle, P. & Chabrier, G. 2008, *ApJ*, 684, 395
- Huang, Y., Zhu, W., & Kokubo, E. 2024, *ApJ*, 975, L38
- Hunter, J. D. 2007, *Computing in Science & Engineering*, 9, 90
- Johnson, S. A., Penny, M., Gaudi, B. S., et al. 2020, *AJ*, 160, 123
- Joncour, I., Duchêne, G., Moraux, E., & Motte, F. 2018, *A&A*, 620, A27
- Koekemoer, A. M., Aussel, H., Calzetti, D., et al. 2007, *ApJS*, 172, 196
- Konopacky, Q. M., Ghez, A. M., Rice, E. L., & Duchêne, G. 2007, *ApJ*, 663, 394
- Kraus, A. L. & Hillenbrand, L. A. 2012, *ApJ*, 757, 141
- Kraus, A. L., White, R. J., & Hillenbrand, L. A. 2006, *ApJ*, 649, 306
- Lafrenière, D., Marois, C., Doyon, R., Nadeau, D., & Artigau, É. 2007, *ApJ*, 660, 770
- Langeveld, A. B., Scholz, A., Mužić, K., et al. 2024, *AJ*, 168, 179
- Lazzoni, C., Rice, K., Zurlò, A., Hinkley, S., & Desidera, S. 2024, *MNRAS*, 527, 3837
- Lucas, P. W. & Roche, P. F. 2000, *MNRAS*, 314, 858
- Luhman, K. L. 2024, *AJ*, 168, 230
- Luhman, K. L., Allers, K. N., Jaffe, D. T., et al. 2007, *ApJ*, 659, 1629
- Luhman, K. L., Alves de Oliveira, C., Baraffe, I., et al. 2024, *AJ*, 167, 19
- Luhman, K. L., Mamajek, E. E., Allen, P. R., Muench, A. A., & Finkbeiner, D. P. 2009, *ApJ*, 691, 1265
- Martín, E. L., {Ž}erjal, M., Bouy, H., et al. 2024, *arXiv e-prints*, arXiv:2405.13497
- Medina, J., Mack, J., & Calamida, A. 2022, *WFC3/UVIS Encircled Energy, Instrument Science Report WFC3 2022-2*, 23 pages
- Miret-Roig, N., Bouy, H., Raymond, S. N., et al. 2022, *Nature Astronomy*, 6, 89
- Mróz, P., Poleski, R., Han, C., et al. 2020, *AJ*, 159, 262
- Mróz, P., Udalski, A., Skowron, J., et al. 2017, *Nature*, 548, 183
- Mužić, K., Scholz, A., Geers, V., Fissel, L., & Jayawardhana, R. 2011, *ApJ*, 732, 86
- Mužić, K., Scholz, A., Geers, V. C., & Jayawardhana, R. 2015, *ApJ*, 810, 159
- Ochsenbein, F., Bauer, P., & Marcout, J. 2000, *A&AS*, 143, 23
- Offner, S. S. R., Moe, M., Kratter, K. M., et al. 2023, in *Astronomical Society of the Pacific Conference Series*, Vol. 534, *Protostars and Planets VII*, ed. S. Inutsuka, Y. Aikawa, T. Muto, K. Tomida, & M. Tamura, 275
- Padoan, P. & Nordlund, Å. 2004, *ApJ*, 617, 559
- Palau, A., Huélamo, N., Barrado, D., Dunham, M. M., & Lee, C. W. 2024, *New A Rev.*, 99, 101711
- Parker, R. J. & Quanz, S. P. 2012, *MNRAS*, 419, 2448
- Peña Ramírez, K., Béjar, V. J. S., Zapatero Osorio, M. R., Petr-Gotzens, M. G., & Martín, E. L. 2012, *ApJ*, 754, 30
- Plotly Technologies Inc. 2015, *Collaborative data science*
- Portegies Zwart, S. & Hochar, E. 2024, *SciPost Astronomy*, 3, 001
- Preibisch, T. & Zinnecker, H. 1999, *AJ*, 117, 2381
- Price-Whelan, A. M., Sipőcz, B. M., Günther, H. M., et al. 2018, *AJ*, 156, 123
- Pueyo, L. 2016, *ApJ*, 824, 117
- Ratzenböck, S., Großschedl, J. E., Alves, J., et al. 2023, *A&A*, 678, A71
- Reipurth, B. 2008a, *Handbook of Star Forming Regions, Volume I: The Northern Sky*, Vol. 4
- Reipurth, B. 2008b, *Handbook of Star Forming Regions, Volume II: The Southern Sky*, Vol. 5
- Reipurth, B. & Clarke, C. 2001, *AJ*, 122, 432
- Ren, B., Pueyo, L., Zhu, G. B., Debes, J., & Duchêne, G. 2018, *ApJ*, 852, 104
- Robitaille, T. 2019, *APLpy v2.0: The Astronomical Plotting Library in Python*
- Robitaille, T. & Bressert, E. 2012, *APLpy: Astronomical Plotting Library in Python, Astrophysics Source Code Library*
- Romero, J. O. 2019, *olivares-j/Sakam: Basic functionality*
- Ruffio, J.-B., Macintosh, B., Wang, J. J., & Pueyo, L. 2017, in *Society of Photo-Optical Instrumentation Engineers (SPIE) Conference Series*, Vol. 10400, *Society of Photo-Optical Instrumentation Engineers (SPIE) Conference Series*, ed. S. Shaklan, 1040027
- Ryu, Y.-H., Mróz, P., Gould, A., et al. 2021, *AJ*, 161, 126
- Schneider, A. C., Windsor, J., Cushing, M. C., Kirkpatrick, J. D., & Wright, E. L. 2016, *ApJ*, 822, L1
- Scholz, A., Jayawardhana, R., Muzic, K., et al. 2012, *ApJ*, 756, 24
- Soummer, R., Pueyo, L., & Larkin, J. 2012, *ApJ*, 755, L28
- Stetson, P. B. 1987, *PASP*, 99, 191
- Strampelli, G. M., Pueyo, L., Aguilar, J., et al. 2022, *AJ*, 164, 147
- Sumi, T., Koshimoto, N., Bennett, D. P., et al. 2023, *AJ*, 166, 108
- Tamura, M., Itoh, Y., Oasa, Y., & Nakajima, T. 1998, *Science*, 282, 1095
- Tange, O. 2011, *login: The USENIX Magazine*, 36, 42
- Taylor, M. B. 2005, in *Astronomical Society of the Pacific Conference Series*, Vol. 347, *Astronomical Data Analysis Software and Systems XIV*, ed. P. Shopbell, M. Britton, & R. Ebert, 29
- Todorov, K., Luhman, K. L., & McLeod, K. K. 2010, *ApJ*, 714, L84
- Todorov, K. O., Luhman, K. L., Konopacky, Q. M., et al. 2014, *ApJ*, 788, 40
- Veras, D. & Raymond, S. N. 2012, *MNRAS*, 421, L117
- Wang, J. J., Ruffio, J.-B., De Rosa, R. J., et al. 2015a, *pyKLIP: PSF Subtraction for Exoplanets and Disks*, *Astrophysics Source Code Library*, record ascl:1506.001
- Wang, L., Kouwenhoven, M. B. N., Zheng, X., Church, R. P., & Davies, M. B. 2015b, *MNRAS*, 449, 3543
- Wang, Y., Perna, R., & Zhu, Z. 2024, *Nature Astronomy*, 8, 756
- Weaver, J. R., Kauffmann, O. B., Ilbert, O., et al. 2022, *ApJS*, 258, 11
- Whitworth, A. P. & Zinnecker, H. 2004, *A&A*, 427, 299
- Wright, E. L., Eisenhardt, P. R. M., Mainzer, A. K., et al. 2010, *AJ*, 140, 1868
- Yu, F. & Lai, D. 2024, *ApJ*, 970, 97
- Zapatero Osorio, M. R., Béjar, V. J. S., Martín, E. L., et al. 2000, *Science*, 290, 103

**Table 4.** HST Targets

Object ID	RA (J2000) (deg)	Dec (J2000) (deg)	Mass ( $M_{\text{Jup}}$ )	i (mag)	$\sigma_i$ (mag)	z (mag)	$\sigma_z$ (mag)	F814W (mag)	$\sigma_{F814W}$ (mag)	F850LP (mag)	$\sigma_{F850LP}$ (mag)	J (mag)	$\sigma_J$ (mag)
Taurus													
J041514.73+280009.0	63.81145	28.00243	22	19.88	0.05	18.13	0.05	18.67	0.01	17.54	0.01	15.07	0.05
J041546.22+280811.4	63.94261	28.13649	6	26.26	0.21	23.47	0.05	24.77	0.21	23.7	0.25	19.96	0.14
...													
J041548.09+291132.9	63.95039	29.19245	23	20.62	0.05	18.92	0.05	19.52	0.01	18.34	0.01	15.7	0.05
J041947.39+281534.6	64.94751	28.25954	7	23.02	0.05	21.53	0.05	22.27	0.04	21.05	0.04	18.15	0.05
Upper Scorpius													
J154540.24-242207.2	236.41761	-24.36874	8	23.41	0.1	21.99	0.07	22.9	0.06	21.9	0.07	18.55	0.06
J154915.32-244139.1	237.31381	-24.69425	8	22.92	0.05	21.27	0.05	22.07	0.03	21.04	0.04	18.2	0.06
...													
J155150.21-213457.4	237.95917	-21.58269	9	23.09	0.05	21.28	0.05	22.27	0.04	21.23	0.04	18.21	0.06
J155416.68-263018.1	238.56942	-26.50513	9	22.27	0.05	20.62	0.05	21.5	0.02	20.46	0.02	17.58	0.05

**Notes.** Full table available in electronic format.

**Table 5.** VLT targets

Object ID	RA (J2000) (deg)	Dec (J2000) (deg)	Mass ( $M_{\text{Jup}}$ )	i (mag)	$\sigma_i$ (mag)	z (mag)	$\sigma_z$ (mag)	J (mag)	$\sigma_J$ (mag)	strehl (%)
793	243.58935	-23.65409	21	18.63	0.05	17.37	0.05	14.99	0.05	2
924	244.96433	-22.69256	28	18.45	0.05	17.03	0.05	14.42	0.05	3

**Notes.** ID, masses and photometry from Miret-Roig et al. (2022). Full table available in electronic format.



## Appendix A: HST Photometry

We performed aperture photometry for all targets using the `photutils` Python package (Bradley et al. 2025), adopting an aperture size of  $0''.16$  and a background annulus between  $0''.25$  and  $0''.50$ . Finite-to-infinite aperture corrections provided by Medina et al. (2022) were applied to all measurements. Photometric uncertainties were calculated following the method outlined in Stetson (1987), accounting for Poisson noise, sky background noise, and readout noise.

For the  $0''.11$  binary J042705.86+261520.3, a larger aperture of  $0''.44$  was employed to include both components, along with a background annulus between  $0''.44$  and  $0''.6$ . The corresponding finite-to-infinite aperture correction from Medina et al. (2022) was applied. The fluxes of the individual components were subsequently derived by measuring the flux ratio in each filter.

Finally, instrumental fluxes were converted to AB magnitudes using the formula specified in the instrument manual.:

$$\text{ABmag} = -2.5 \times \log_{10}(\text{Flux} \times \text{PHOTFLAM} - 21.10 - 5 \times \log_{10}(\text{PHOTPLAM}) + 18.6921) \quad (\text{A.1})$$

where `PHOTFLAM` is the bandpass unit response and `PHOTPLAM` is the bandpass pivot wavelength (in angstroms), both provided by STScI in the FITS image headers. Figure 9 shows the (F814W, F814W-F850LP) color-magnitude diagrams for the two samples.